Semiconductor Science
and Technology

PAPER

Tunable p- and n-type Nb:TiO_2 and performance optimizing of self-powered Nb:TiO_2/CdS photodetectors

To cite this article: Dawei Wang *et al* 2020 *Semicond. Sci. Technol.* **35** 075015

IOP Publishing Semiconductor Science and Technology
Semicond. Sci. Technol. **35** (2020) 075015 (7pp) https://doi.org/10.1088/1361-6641/ab883d

Tunable p- and n-type Nb:TiO_2 and performance optimizing of self-powered Nb:TiO_2/CdS photodetectors

Dawei Wang, Haibiao Chen, Yuxin Min, Jun Liang[1] and Feng Pan[1]

School of Advance Materials, Peking University Shenzhen Graduated School, 2199 Lishui Road, Shenzhen 518055, People's Republic of China

E-mail: liangjun@pkusz.edu.cn and panfeng@pkusz.edu.cn

Received 12 February 2020, revised 19 March 2020
Accepted for publication 9 April 2020
Published 12 June 2020

Abstract

For the first time, Niobium-doped titanium dioxide (Nb:TiO_2, NTO) and cadmium sulfide (CdS) are selected for building self-powered photodetectors for optimizing the performance. The p- or n-type NTO and the band structures of the heterojunctions can be controlled by doping Nb and tuning the sputtering power. A low sputtering power tends to produce pure anatase crystals and a high power induces an additional rutile phase aligned in the (200) orientation. NTO films deposited at a sputtering power of 120 W show p-type behavior attributed to the compensation of oxygen vacancies. NTO films deposited at 180 W contain mixed anatase and rutile phases with lattice imperfections and show n-type semiconductor properties after annealing. By measuring the energy band structure of the n-n-type anatase-TiO_2/CdS, p-n-type anatase-NTO/CdS, and n-n-type mix-NTO/CdS heterojunctions, we identify the interface carrier motion characteristics and tune the energy band structure to optimize the performance of the photodetectors. Without any external power supply, the responsivities reach at least 0.125A/W in the mix-NTO/CdS (light source: 550 nm) and the response speed is lower than 10 ms, which can be used for building a self-powered photodetector.

Supplementary material for this article is available online

Keywords: photodetector, TiO_2, self-powered

(Some figures may appear in colour only in the online journal)

1. Introduction

Photodetectors are widely used in photo-communication systems and photoelectric sensors [1]. At present, research targets in improving existing photodetectors to achieve high photosensitivity [2–4], high gain and high response speed [3, 5], and other functions such as flexibility [6, 7], transparency [8] and self-power [9–19]. Among these features, self-powered photodetectors, which work without an external power source including those based on the Schottky junction, p–n junction, photoelectrochemical cell, and nanogenerators in the integrated nanosystem [20], have attracted great attentions for their ultrahigh switch ratio, continuously working and a character of energy-saving [21–23]. It is a promising task to develop self-powered photodetectors with high photocurrent, high response speed, chemical stability, low cost and good manufacturability.

As a wide bandgap semiconductor, titanium dioxide (TiO_2) has attracted great attention for its particular advantages of rich abundance, low-cost, temperature stability and chemical stability [24]. Cadmium sulfide (CdS) is widely used as an n-type photosensitive semiconductor material in optoelectronic devices [25–30]. In a TiO_2/CdS heterojunction structure, TiO_2 can promote the separation of photon-generated electron-hole pairs from CdS [31, 32]. TiO_2/CdS heterojunction has been confirmed to be able to perform photoelectric conversion. But most of the research on TiO_2/CdS heterojunctions in the past were focused on the photo-catalyst or the solar

[1] Author to whom any correspondence should be addressed.

cells applications because of not preparing a device with high on/off ratio and a high response speed.

In this work, we use the tunable carrier of NTO (Nb:TiO_2, NTO) to fabricate self-powered photodetectors with NTO/CdS heterojunction structure. In the end, the n-n type NTO/CdS device achieved high response speed, for the advance of the n-n-type heterojunction, which does not have a depletion region that the drift current of the carriers is much larger than the recombination current [33].

Pure TiO_2 is usually an n-type semiconductor due to the presence of oxygen vacancies. Peng *et al* used the high power sputter deposition to form p-type TiO_2 films [34]. Interestingly, we found previously that p-type TiO_2 films can be deposited by using a relatively low sputtering power, which can be used for mature photodetectors fabrication process. In addition, our previous work of NTO aimed to the transparent conductive oxide (TCO) with resistance lower than $10^{-4}(\Omega\text{cm})$ [35, 36], but the high carrier density leads to a metallic behavior so it is not suitable for the junction. Here we prepared three kinds of TiO_2-based films using pure TiO_2 and two kinds of Nb:TiO_2 (n- and p-type NTO, respectively) materials by flowing a small amount of oxygen during sputtering for tuning the conductivity. As a result, the NTO films showed a semiconductive property. These n- and p-type NTO materials were deposited with controlling the phase to be pure anatase phase or anatase-rutile mixed phase, respectively. The sputtering power for pure anatase sample was 120 W, and the sputtering power for mixed phases was 180 W. In heterojunctions of these three kinds of TiO_2-based films and CdS, the direction of the self-photocurrent in the device prepared with the n-type NTO of the anatase-rutile mixed phase is opposite to that in the devices prepared with the pure anatase TiO_2 and anatase p-type NTO. By x-ray photoelectron spectroscopy (XPS), we revealed the pattern of carrier motion at the interface between n-type NTO, p-type NTO or pure TiO_2 and CdS and the mechanism to form a p-NTO or n-NTO film. The TiO_2/CdS was found to be a direct Z-scheme heterojunction and the p-type NTO/CdS or n-type NTO/CdS were Type-II heterojunctions. The x-ray diffraction (XRD) measurements indicate that the evolution of the NTO from the anatase phase to the anatase-rutile mixed phase is due to the higher power that enhances the impact energy during film sputtering, causing the spacing of the (003), (004), (112) planes to be compressed and the structure gradually evolve into a rutile (200) phase. The self-powered photodetectors are highly responsive to the visible light with wavelengths below 550 nm, and highly transparent to the light above 550 nm. The average light transmittance from 550 nm to 800 nm exceeds 75%. Without an external power supply, the light current reaches 2000 nA (0.125 W A^{-1}) in the n-n-type NTO/CdS under a relatively long wave (550 nm optical source) illumination and the response speed is lower than 10 ms.

2. Experimental section

2.1. Deposition procedure

The FTO glass was purchased from GULUO GLASS. All the TiO_2 or NTO films were deposited by vacuum magnetron sputtering, using a pure TiO_2 target or Nb:TiO_2 targets with 5% atom of Nb dopant (Ti0.95Nb0.05O2, 99.9%, Hzamtarget). The soda-lime glass substrate (GULUO GLASS) and the FTO glass (GULUO GLASS) were simultaneously used as the substrates. The films are deposited by PeiKing ZhongKeDeSheng TVC3000 vacuum magnetron sputtering system. The angle between the target and the substrate glass was about 60 degrees, and the substrate was rotated at a constant speed of 10 r min^{-1}. The air pressure was maintained at 0.25 Pa during sputtering with an argon flow rate of 50 sccm and oxygen flow rate of 2 sccm. The 120 W NTO&TiO_2 was sputtered at a 0.27 A current and a 450 V voltage. The 180 W NTO was sputtered at a 0.39 A current and a 470 V voltage. The annealing was taken in a tube furnace about 60 min at 400 °C with Ar. A CdS film of about 500 nm was obtained by RF magnetron sputtering at a power of 25 W. Then the FTO/NTO/CdS film or the FTO/TiO_2/CdS film was placed in a muffle furnace and annealed at 400 °C for 20 min for crystallization at the heterojunction interface.

2.2. Characterization and measurements method

First we draw a circuit with silver paste on the print circuit board (PCB) and put the chip upside-down to form a contact. The voltage-current text and the time-current test are measured by Tektronix B4200 and the high-resolution time-current test are measured by Aglient B1500A semiconductor analyser. Photoelectron spectroscopy were performed by the Thermo Fisher ESCALAB 250X equipped with a monochromatized Al anode x-ray source (x-ray photoelectron spectroscopy, XPS, $h\upsilon = 1486.6$ eV). The crystal structure of the films were analyzed with a Bruker D8 Advance powder x-ray diffractometer (XRD) equipped with CuKα radiation with a two-dimensional detector. The thickness of films were observed with a Zeiss SUPRA-55 Scanning Electron Microscope (SEM). Microstructures were observed by a JEOL JEM2010-FEF high resolution transmission electron microscope (HRTEM). The cross-section of the NTO or TiO_2 films for TEM observation were prepared by FEI Scios focused-ion-beam (FIB) and the structures were coated with a Pt protective layer and then a lamella was cut out and lifted off on a copper grid. The lamellas were thinned down to 100 nm using 100 pA current under 30 kV acceleration voltage and then polished down to 50 nm using 8 pA under 2 kV.

3. Results and discussion

Figure 1 shows the structure of the photodetectors. The films were grown by the vacuum magnetron sputtering on the FTO (F:SnO_2) glass and the thickness of the TiO_2 or NTO films are all about 150 nm. The heterojunction area is 2×2 mm^2. For the convenience of testing, we used silver paste as the electrodes to connect the CdS and the FTO to the circuit board which leads to the testing probes.

X-ray diffraction (XRD) was used to characterize the crystallization of TiO_2 and NTO films on the glass substrate and the results are shown in figure 2(a). It can be seen that the TiO_2 film and the NTO film sputtered at 120 W exhibit a typical

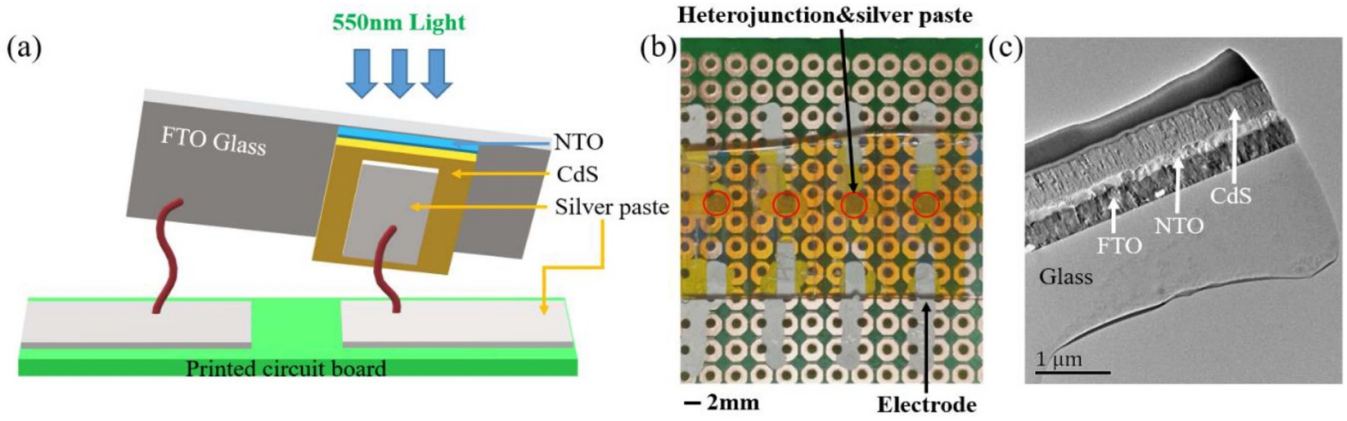

Figure 1. (a) Device structure diagram, the light is injected from the back of the glass. (b) The real devices with silver paste connection on the circuit board (in the red circles). (c) Transmission electron microscope (TEM) image of the cross-section of the device.

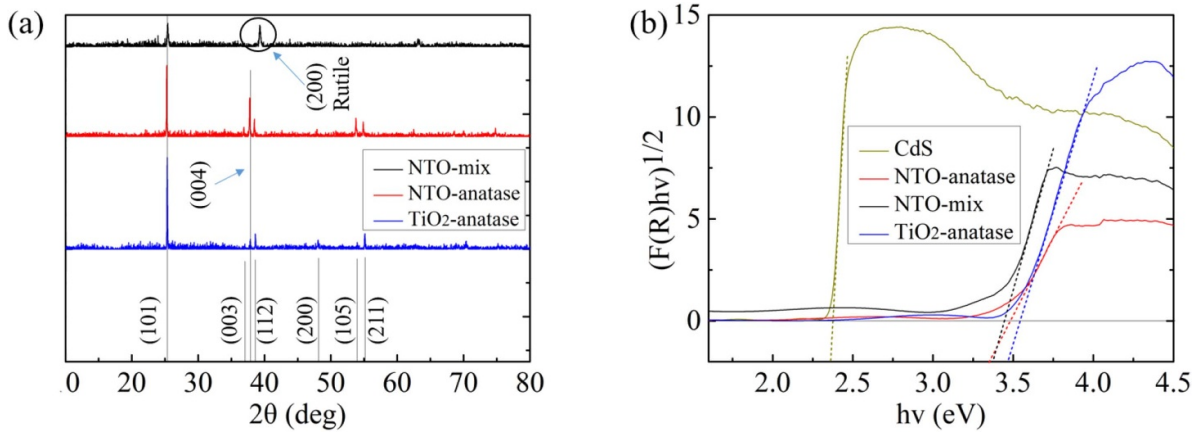

Figure 2. (a) The x-ray diffraction text (XRD) of a single layer about 120 W- anatase-TiO_2, 120 W-anatase-NTO, and 180 W-mix-NTO. (b) The optical bandgaps (OBG) of 120 W-anatase-TiO_2, 120 W-anatase-NTO, 180 W-mix-NTO and CdS films.

pure phase of anatase. For the NTO film sputtered at 120 W, the (101) and (004) peaks shift to low angles by about 0.1° and 0.15°, respectively. This is because the Nb atom substituted for Ti and it is in the original position of Ti, without altering the crystal structure. However, since the atomic radius of Nb is slightly larger than Ti, the peak position shifted a little due to the dilation of the unit cell. For the mix-NTO film sputtered at 180 W, the (101) anatase peak was still present but the (003), (004), (112) peaks disappeared. We prepared NTO at 150 W sputtering power to observe the evolution of the crystal type as the sputtering power changed from 120 W to 180 W, and the results are shown in the supporting information figure S1 stacks.iop.org/SST/35/075015/mmedia. When the power was increased to 150 W, the (003), (004), and (112) peaks all shifted to the right by 0.6 degrees, but the crystal was still anatase phase. When the power was increased to 180 W, these three peaks disappeared and replaced by the peak of the rutile phase (200) at 39.2°. This evolution can be tentatively explained by that when the power was increased from 120 W to 150 W, some crystal orientations in the material were compressed due to the increased kinetic energy of the impacting particles. However, the material remains anatase after annealing. When the sputtering power was close to 180 W, the further compress and the run off of oxygen impels the crystal lattice transformed into a rutile phase and the monolithic film exhibits particular mixed phases of anatase and rutile. We presume the reason is that the pure anatase phase in anatase-NTO is Ti-deficient during the period of sputtering deposition and Nb element could not effectively substitute for Ti in NTO, while the mix-NTO sputtered at 180 W was supplied with a sufficient Ti content and Nb substitute more effectively at a high sputtering power. We cannot continue to prepare samples with a power greater than 180 W because the limitation of our magnetron sputtering equipment.

Figure 2(b) shows the optical bandgaps (OBG) of three TiO_2-based films and the CdS film by constructing the Tauc plots using the ($\alpha h\nu$) power 1/2 relation method. The relevant diffusive reflection data and the Kubelka-Munk conversion from reflectance to absorbance are in the supporting information figure S2. The transmittance measurements of the TiO_2-based/CdS complex films and single TiO_2-based films are shown in the supporting information figure S3 respectively. It can be seen that the forbidden bandwidths of 120 W-anatase-TiO_2, 120 W-anatase-NTO, 180 W-mix-NTO and CdS are 3.54 eV, 3.48 eV, 3.45 eV and 2.37 eV, respectively. It can be seen that the forbidden bandwidth of TiO_2 is reduced by 0.06 eV after doping Nb, and the bandgap of the mixed phase sample sputtered at 180 W is further reduced. These

forbidden bandwidth data will be used for subsequent band structure analysis.

The Hall coefficient of the anatase-NTO film and the mix-NTO film are +6.59 ($cm^3\,C^{-1}$) and −8168 ($cm^3\,C^{-1}$), respectively, which indicates that the 120 W-anatase-NTO film is a weak p-type semiconductor and the 180 W-mix-NTO film is a strong n-type semiconductor. The resistivities of 120 W-anatase-NTO and 180 W-mix-NTO are 6.15 (Ωcm) and 6.31 (10^{-3} Ωcm), respectively. However, the electrical properties of the 120 W-anatase-TiO_2 film cannot be measured for its extremely high resistance. The energy band characteristics analyzed by x-ray photoelectron spectroscopy (XPS) in figure 3 also indicate that the 120 W-anatase-NTO film is p-type as discussed below.

XPS was used to get the valence state of Ti and the results are shown in figures 3(a)–(c). The single layers of CdS, TiO_2 or NTO were etched by Ar^+ for 10 s to clean the surface. All the binding energy values were calibrated by the carbon 1 s peak position in the respective sample as reference. In figure 3(a), the peaks at 458.52 eV and 464.21 eV are closed to the XPS reference peaks of Ti 2p3/2 and the Ti 2p1/2, respectively. In figure 3(b), these peaks move to 458.39 eV and 464.12 eV, respectively, and in figure 3(c) they move to 458.05 eV and 463.61 eV, respectively. At the same time, the ratios between the areas of Ti^{3+}/Ti^{4+} peaks in the 120 W-anatase-TiO_2, 120 W-anatase-NTO and 180 W-mix-NTO are 0.32, 0.52 and 1.04, respectively. The Nb 3d peaks of the 120 W-anatase-NTO and the 180 W-mix-NTO are shown in the supporting information figure S4 and the ratio between the peak areas of Nb^{5+}/Nb^{4+} is 0.56 for the 120 W-anatase-NTO and 0.98 for the 180 W-mix-NTO. After Nb doping, the presence of the lower-valence titanium (Ti^{3+}) content can be attributed to the compensating mechanism from the redundant electrons from Nb [35, 36]. It can be seen a higher content of Ti^{3+} in NTO than pure TiO_2 under 120 W. Although the effect of Ti^{2+} on p-type TiO_2 was previously reported, this is not the case here since no Ti^{2+} was found in our XPS and TEM analyses (supporting information figure S5). The proportion of Ti, O and Nb (P_{Ti}, P_O, P_{Nb}) are shown in the supporting information table S6. The density-functional theory (DFT) shows that the TiO_2 is a p-semiconductor under the ideal conditions [35]. But it always acted as an n-semiconductor due to the oxygen vacancies in the actual state. We speculate that the semiconductive properties of NTO is determined by the competition of three factor: oxygen vacancies as n doping for NTO; Nb^{5+} substituting Ti^{4+} (3p orbit), the extra one electron in 4p orbit of Nb^{5+} as n doping, and Ti^{3+} (3d orbit) induced polarization by Nb substituted as p doping [34, 37, 38]. An increase in the Nb content and an effective Nb^{5+} doping in NTO are favored by increasing the sputtering power. At 120 W, although the content of Ti^{3+} in NTO is low, the Nb^{5+} content is even lower, in comparison to 180 W. Furthermore, NTO sputtered at 120 W contains a relatively higher oxygen content to compensate the oxygen vacancies and it shows p-type characteristics, while NTO sputtered at 180 W shows n-type characteristics.

For the interface energy band measurement by the XPS, first a 100 nm CdS film was sputtered on the TiO_2 or NTO surface, after annealed at 400 °C for 20 min, the CdS film was etched away by Ar^+ on the XPS instrument so that the trace of Ti 2p and Cd 3d can be simultaneously got, which is consistent with the literatures [35, 36]. To calculate the energy band structure of their interface in the figures 3(g)–(i), the valence band offset (ΔE_V) were calculated first by formula 1, 2 below [39, 40].

$$\Delta E_v = \left(E_{Ti2p_{\frac{3}{2}}} - E_{VBM}^{TiO_2}\right)_{TiO_2} - \left(E_{Cd3d_{\frac{5}{2}}} - E_{VBM}^{CdS}\right)_{CdS} - \Delta E_{CL} \quad (1)$$

$$\Delta E_{CL} = \left(E_{Ti2p_{\frac{3}{2}}}^{TiO_2} - E_{Cd3d_{\frac{5}{2}}}^{CdS}\right)_{Interface}. \quad (2)$$

For the formula 1 the valence band maximum (E_{VBM}) and the $E_{Ti2p3/2}$ of the 120 W-anatase-TiO_2, 120 W-anatase-NTO and 180 W-mix-NTO films were measured from figures 3(a)–(c). The values of $(E_{Ti2p3/2}\text{-}E_{VBM})_{TiO2}$ or $(E_{Ti2p3/2}\text{-}E_{VBM})_{NTO}$ of the 120 W-anatase-TiO_2, 120 W-anatase-NTO and 180 W-mix-NTO films are 456.13 eV, 456.36 eV, and 455.78 eV, respectively. A value of 403.7 eV was used for $(E_{Cd3d5/2}\text{-}E_{VBM})_{CdS}$, as measured in the supporting information figure S7. ΔE_{CL} in formula 1, 2 is the difference in the binding energy between Ti 2p3/2 and Cd 3d5/2, as shown in figures 3(d)–(f).

The energy band structures of the 120 W-anatase-TiO_2/CdS, 120 W-anatase-NTO/CdS and 180 W-mix-NTO/CdS interface are shown in figures 3(g)–(i), respectively. The bandgap (E_{BG}) of the 120 W-anatase-TiO_2, 120 W-anatase-NTO, 180 W-mix-NTO and CdS have been shown in figure 2(b). Here we did not further calculate the conduction band offset (ΔE_C) using the bandgaps of CdS and TiO_2 or NTO because the interfaces are not ideal heterojunction with abrupt transition due to the diffusion of sulfur during the thermal annealing and the bandgap of TiO_2 narrow down gradually [41–43] and the diffusion at the interfaces are shown by TEM-EDS line scanning in supporting information figures S8 and S9. In addition, the figures S8 and S9 also show that the diffusion at NTO/CdS is more evident than the TiO_2/CdS. The diffusion length of TiO_2/CdS and NTO/CdS are about 10 nm and 35 nm, respectively.

From the energy band structures we can see that the valance band of 120 W-anatase-TiO_2 is lower than that of CdS by 1.18 eV at the interface. The pure TiO_2 has an extremely high resistance that is beyond our measurement capability, so it is difficult to transport the carriers in pure TiO_2 film. It is possible that the anatase-TiO_2/CdS is a direct tunnel heterojunction following the Direct Z-scheme mechanism [44, 45]. The Direct Z-scheme heterojunction produces a high photocurrent even with 150 nm high resistive TiO_2 film. In the energy band of the anatase-NTO, the valance band shifts up and it is lower than that of the CdS by 0.47 eV. In contrast to the anatase-NTO/CdS, the valance band of the mix-NTO moves down and it is lower than the CdS by 1.34 eV. From the directions of the photocurrent we can confirm that the n-n-type mix-NTO/CdS and the p-n-type anatase-NTO/CdS are both Type-II heterojunctions.

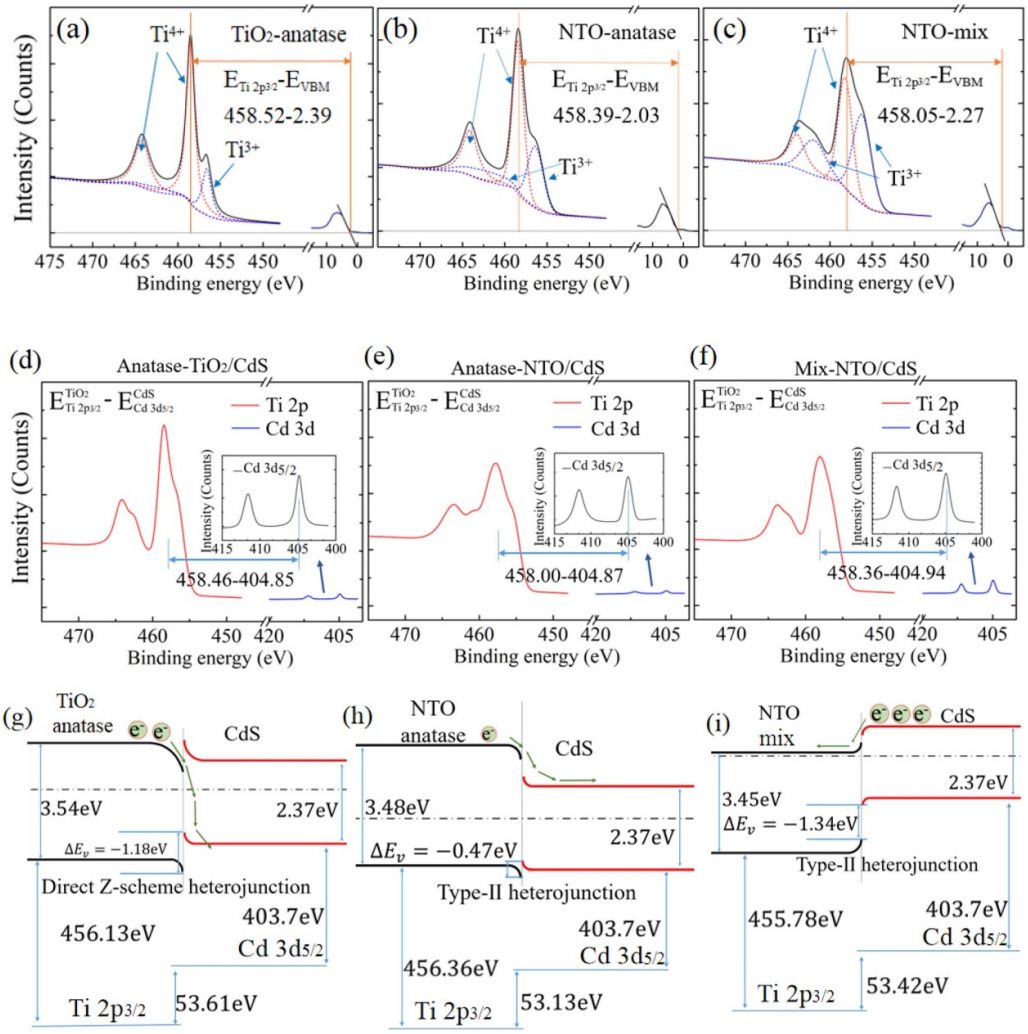

Figure 3. (a), (b), (c) The x-ray photoelectron spectroscopy (XPS) surface characterization of the 120 W-anatase-TiO_2, 120 W-anatase-NTO and 180 W-mix-NTO film, the data was fitted with a Shirley background and individual Gaussian/Lorentzian functions. (d), (e), (f) The XPS interface analysis of the 120 W-anatase-TiO_2/CdS, 120 W-anatase-NTO/CdS and 180 W-mix-NTO/CdS. (g), (h), (i) The energy band structure of the interface in 120 W-anatase-TiO_2/CdS, 120 W-anatase-NTO/CdS and 180 W-mix-NTO/CdS.

Figure 4 is the comparison between the light current (I_{light}) and dark current (I_{dark}) from −0.1 V to 0.1 V under a 400 μW cm^{-2}, 550 nm light. From figures 4(a)–(c) we can see that when the applied voltage shifts to 0 V, the self-photocurrent of the device is positive in figures 4(a), (b) but negative in figure 4(c). The corresponding I_{light} in figures 4(a)–(c) at 0 V are 684 nA, 133 nA and 2005 nA (0.125A/W), respectively. By the way, the long wave 550 nm is not the best wavelength for getting the highest photocurrent but it is valuable for energy saving. The 440 nm response is in the supporting information figure S10. From figures 4(d)–(f) we can see doping Nb into TiO_2 (NTO) increases the dark current by an order of magnitude higher than the pure TiO_2. The dark current indicates that the device fabricated using NTO has a much lower internal resistance than the pure TiO_2.

The response speed of the three kinds of devices switched between the light and the dark conditions are shown in figures 5(a)–(c). Figure 5(d) shows the comparison of these three devices at a higher time resolution. The initial current rises in 120 W-anatase-TiO_2/CdS n-n heterojunction took about 105 ms, and that in the 120 W-anatase-NTO/CdS p-n heterojunction took about 28 ms, while in the 180 W-mix-NTO/CdS n-n heterojunction it took less than 10 ms (The time resolution of B1500 is 10 ms). The prior reports is in the supporting information table S11.

For the p-type 120 W-anatase-NTO/CdS device, the photocurrent is small due to the lower carrier concentration of NTO. In contrast, the n-type 180 W-mix-NTO has a significant electron concentration superiority and presents high density of photo current of the photodetector. With little electron-hole recombination, the n-n-type heterojunction prepared by mix-NTO is almost dominant solely by the drift current of the carrier in the light response, and the response speed is increased significantly. Although for now the p-type NTO did not show the best performance in photodetector due to its high resistivity, considering its wide bandgap (∼3.5 eV), it could be used in wide bandgap semiconductor devices and chips.

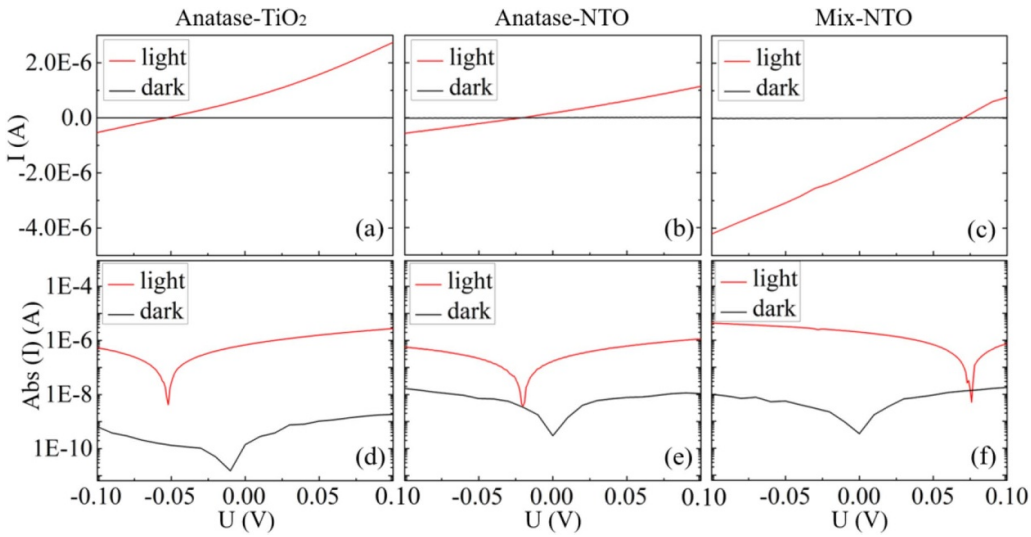

Figure 4. The I_{light} and I_{dark} from −0.1 V to 0.1 V at a 400 μW cm^{-2}, 550 nm light. (a), (d) The device made from 120 W-anatase-TiO_2/CdS. (b), (e) The device made from 120 W-anatase-NTO/CdS. (c), (f) The device made from 180 W-mix-NTO/CdS.

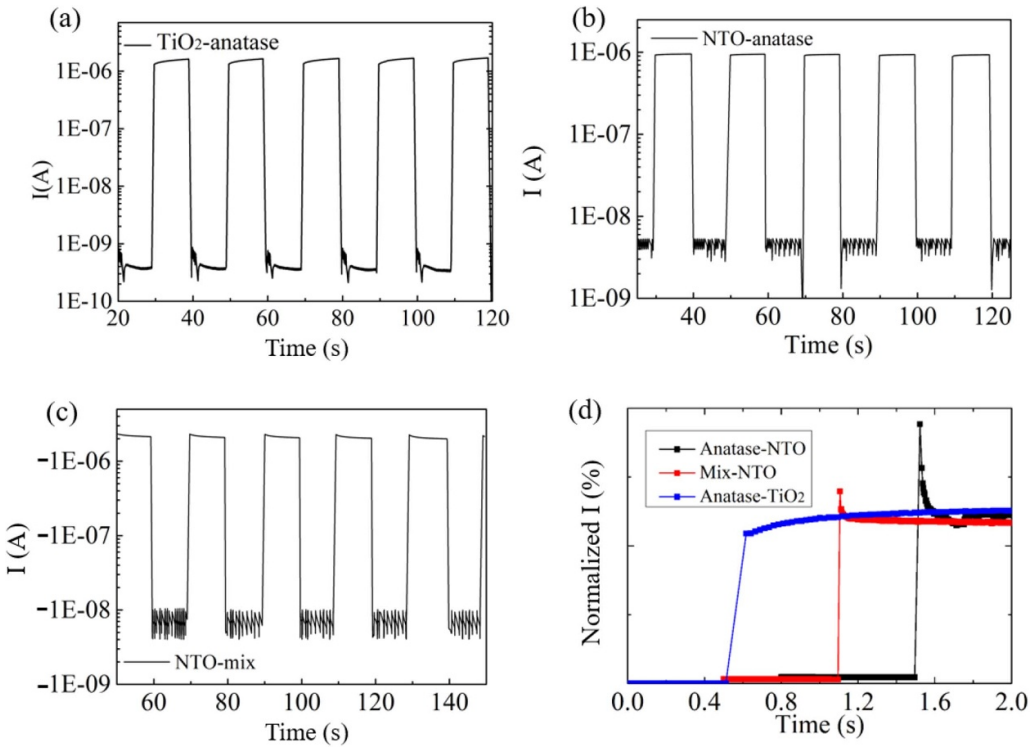

Figure 5. The response speed of the three kinds of devices. (a) The 120 W-anatase-TiO_2/CdS device. (b) The 120 W-anatase-NTO/CdS device. (c) The 180 W-mix-NTO/CdS device. (d) The high time resolution of response speed of three devices with normalized current.

4. Conclusion

We achieve to selectively deposit n- or p-type Nb:TiO_2 (NTO) thin films by adjusting the sputtering power. Three types of TiO_2-based/CdS heterojunctions were fabricated and their performance as photodetectors were evaluated. The device prepared by the n-type mixed phase NTO film deposited at 180 W has characteristics of a higher light current (0.125A/W) and a higher response speed (less than 10 ms). Through the energy band analysis, the reasons for the increased device response speed and the photocurrent enhancement could be explained by optimized conductivity and band alignment. The working mechanism of these devices is supported by the energy band theory for the TiO_2/CdS heterojunction and the p-type and n-type doped TiO_2. These photodetectors can be used in a circuit where energy saving is critical and a high response speed and high photosensitivity are required. Because of its light transmittance capability, it can also be used in a circuit with layered detectors.

Acknowledgments

This work was financially supported by the Shenzhen key science and technology plan (Grant No. JSGG20141118144410953), the Guangdong applied technology research special project (Grant No. 2015B090927003), and the Shenzhen Science and Technology Innovation Committee (Grant No. JCYJ20150331101121646, No. KQJSCX20180323174713505 and No. JCYJ20170818085823773).

ORCID iDs

Jun Liang https://orcid.org/0000-0002-2879-3327
Feng Pan https://orcid.org/0000-0002-8216-1339

References

[1] Deng K and Li L 2014 *Adv. Mater.* **26** 2619
[2] Cao F, Meng L, Wang M, Tian W and Li L 2019 *Adv. Mater.* **31** e1806725
[3] Shen L, Fang Y, Wang D, Bai Y, Deng Y, Wang M, Lu Y and Huang J 2016 *Adv. Mater.* **28** 10794
[4] Xiao P, Mao J, Ding K, Luo W, Hu W, Zhang X, Zhang X and Jie J 2018 *Adv. Mater.* **30** 1801729
[5] Lu Z, Xu Y, Yu Y, Xu K, Mao J, Xu G, Ma Y, Wu D and Jie J 2020 *Adv. Funct. Mater.* **19** 07951
[6] Li Y, Alian A, Sivan M, Huang L, Ang K W, Lin D, Mocuta D, Collaert N and Thean V Y 2019 *APL Mater.* **7** 031503
[7] Han H, Lee C, Kim H and Kim Y 2018 *Adv. Funct. Mater.* **28** 1800704
[8] Rana A K, Kumar M, Ban D K, Wong C P, Yi J and Kim J 2019 *Adv. Electron. Mater.* **5** 1900438
[9] Song K, Ma N, Mishra Y K, Adelung R and Yang Y 2019 *Adv. Electron. Mater.* **5** 1800413
[10] Ji Y, Wang Y and Yang Y 2019 *Adv. Electron. Mater.* **5** 1900195
[11] Chowdhury A M, Chandan G, Pant R, Roul B, Singh D K, Nanda K K and Krupanidhi S B 2019 *ACS Appl. Mater. Interfaces.* **11** 10418
[12] Ghosh J, Natu G and Giri P K 2019 *Org. Electron.* **71** 175
[13] Jia C, Wu D, Wu E, Guo J, Zhao Z, Shi Z, Xu T, Huang X, Tian Y and Li X 2019 *J. Mater. Chem.* C **7** 3817
[14] Sun M, Yang P, Xie D, Sun Y, Xu J, Ren T and Zhang Y 2019 *Adv. Electron. Mater.* **5** 1800580
[15] Md Foisal A R, Dinh T, Nguyen V T, Tanner P, Phan H-P, Nguyen T-K, Haylock B, Streed E W, Lobino M and Dao D V 2019 *IEEE Trans. Electron Devices.* **66** 1804
[16] Huang G, Zhang P and Bai Z 2019 *J. Alloy. Compd.* **776** 346
[17] Wu E, Wu D, Jia C, Wang Y, Yuan H, Zeng L, Xu T, Shi Z, Tian Y and Li X 2019 *ACS Photonics* **6** 565
[18] Wu D, Wang Y, Zeng L, Jia C, Wu E, Xu T, Shi Z, Tian Y, Li X and Tsang Y H 2018 *ACS Photonics* **5** 3820
[19] Wu D *et al* 2019 *ACS Nano* **13** 9907
[20] Tian W, Wang Y, Chen L and Li L 2017 *Small* **13** 1701848
[21] Huang Y, Zhang L, Wang J, Chu X, Zhang D, Zhao X, Li X, Xin L, Zhao Y and Zhao F 2019 *J. Alloy. Compd.* **802** 70
[22] Zhou H, Gui P, Yu Q, Mei J, Wang H and Fang G 2015 *J. Mater. Chem.* C **3** 990
[23] Guo D *et al* 2018 *ACS Nano* **12** 12827
[24] Emeline A V, Furubayashi Y, Zhang X, Jin M, Murakami T and Fujishima A 2005 *J. Phys. Chem.* B **109** 24441
[25] Jung K, Lee J, Kim Y-M, Chang Park Y and Lee M-J 2019 *Compos. Sci. Technol.* **179** 79
[26] Li L, Jin Z, Tao R, Li F, Wang Y, Yang X and Xu L 2019 *J. Photochem. Photobiol.* A **377** 101
[27] Bayhan H, Dağkaldıran E T, Major J D, Durose K and Bayhan M 2019 *Semicond. Sci. Technol.* **34** 075013
[28] Wu C, Jie J, Wang L, Yu Y, Peng Q, Zhang X, Cai J, Guo H, Wu D and Jiang Y 2011 *Nanotechnology* **22** 069801
[29] Meshkov A S, Ostretsov E F, Pogosov W V, Ryzhikov I A and Trofimov Y V 2010 *Semicond. Sci. Technol.* **25** 6
[30] Mutalikdesai A and Ramasesha S K 2017 *Thin Solid Films* **632** 73
[31] Wang M, Zhang H, Zu H, Zhang Z and Han J 2018 *Appl. Surf. Sci.* **455** 729
[32] Zhou P, Le Z, Xie Y, Fang J and Xu J 2017 *J. Alloy. Compd.* **692** 170
[33] Dong Y, Zheng W, Yan X, Dai Y, Zhang X and He G 2019 *J. Mater. Sci., Mater. Electron.* **30** 13099
[34] Peng W C, Chen Y C, He J L, Ou S L, Horng R H and Wuu D S 2018 *Sci. Rep.* **8** 9255
[35] Yang X, Min Y, Li S, Wang D, Mei Z, Liang J and Pan F 2018 *Catal. Sci. Technol.* **8** 1357
[36] Yang X *et al* 2017 *ACS Appl. Mater. Interfaces.* **9** 29021
[37] Liu Y, Szeifert J M, Feckl J M, Mandlmeier B, Rathousky J, Hayden O, Fattakhova-Rohlfing D and Bein T 2010 *ACS Nano* **4** 5373
[38] Peng W C, Chen Y H, Chen J Y, He J L and Wuu D S 2017 *Mater. Sci. Semicond. Process.* **61** 85
[39] Su Y, Xin C, Feng Y, Lin Q, Wang X, Liang J, Zheng J, Lin Y and Pan F 2016 *ACS Appl Mater. Interfaces.* **8** 28143
[40] Kraut E A, Grant R W, Waldrop J R and Kowalczyk S P 1980 *Phys. Rev. Lett.* **44** 1620
[41] Kripal R, Vaish G and Tripathi U M 2019 *J. Electron. Mater.* **48** 1545
[42] Zhou S, Liu S, Su K and Jia K 2019 *J. Alloy. Compd.* **804** 10
[43] Bento R T, Correa O V and Pillis M F 2019 *J. Eur. Ceram. Soc.* **39** 3498
[44] Low J, Dai B, Tong T, Jiang C and Yu J 2019 *Adv. Mater.* **31** e1802981
[45] Wang X, Liu G, Wang L, Pan J, Lu G Q and Cheng H 2011 *J. Mater. Chem.* **21** 869